

Evolution of chirality from transverse wobbling in ^{135}Pr

N. Sensharma,^{1,2,3,*} U. Garg,^{1,†} Q. B. Chen,⁴ S. Frauendorf,¹ S. Zhu,^{5,‡} J. Arroyo,¹ A. D. Ayangeakaa,^{2,3} D. P. Burdette,^{1,§} M. P. Carpenter,⁶ P. Copp,⁶ J. L. Cozzi,^{1,¶} S. S. Ghugre,⁷ D. J. Hartley,⁸ K. B. Howard,^{1,**} R. V. F. Janssens,^{2,3} F. G. Kondev,⁶ T. Lauritsen,⁶ J. Li,⁶ R. Palit,⁹ A. Saracino,^{2,3} D. Seweryniak,⁶ S. Weyhmler,^{1,††} and J. Wu⁶

¹Department of Physics and Astronomy, University of Notre Dame, Notre Dame, IN 46556, USA

²Department of Physics and Astronomy, University of North Carolina Chapel Hill, NC 27599, USA

³Triangle Universities Nuclear Laboratory, Duke University, Durham, NC 27708, USA

⁴Department of Physics, East China Normal University, Shanghai 200241, China

⁵National Nuclear Data Center, Brookhaven National Laboratory, Upton, NY 11973, USA

⁶Physics Division, Argonne National Laboratory, Argonne, IL 60439, USA

⁷UGC-DAE Consortium for Scientific Research, Kolkata 700 064, India

⁸Department of Physics, United States Naval Academy, Annapolis, MD 21402, USA

⁹Department of Nuclear and Atomic Physics, Tata Institute of Fundamental Research, Mumbai 400 005, India

(Dated: March 19, 2024)

Chirality is a distinct signature that characterizes triaxial shapes in nuclei. We report the first observation of chirality in the nucleus ^{135}Pr using a high-statistics Gammasphere experiment with the $^{123}\text{Sb}(^{16}\text{O},4n)^{135}\text{Pr}$ reaction. Two chiral-partner bands with the configuration $\pi(1h_{11/2})^1 \otimes \nu(1h_{11/2})^{-2}$ have been identified in this nucleus. Angular distribution analyses of the $\Delta I = 1$ connecting transitions between the two chiral partners have revealed a dominant dipole character. Quasiparticle triaxial rotor model calculations are in good agreement with the experiment. This is the first time that both signatures of triaxiality–chirality and wobbling–have been observed in the same nucleus.

I. INTRODUCTION

Nuclear chiral rotation is a unique signature that helps in the identification of triaxial nuclear shapes. Chirality appears when the axis of rotation does not lie in any of the three principal planes of the nucleus [1–4]. This arrangement occurs when there is a finite angular momentum component along all three principal axes of a triaxial rotor. Chirality is experimentally manifested as two nearly identical $\Delta I = 1$ sequences with the same parity and close excitation energies. A number of nuclei have been found to exhibit nuclear chiral rotation. Some examples include nuclei in the regions $A \sim 80$ (^{80}Br [5]), $A \sim 100$ (^{104}Rh [6]), $A \sim 130$ (^{135}Nd [7, 8], ^{134}Pr [9–11], ^{128}Cs [12], ^{133}Ce [13]), and $A \sim 190$ (^{188}Ir [14]). A comprehensive compilation can be found in Ref. [15]. In all cases, two $\Delta I = 1$ bands with close excitation energies were reported. The small energy difference between the two bands were attributed to tunneling between the left- and right-handed configurations in the case of static chirality or chiral rotation (CR) [1], and to an oscillation between the two configurations in the case of chiral vibrations (CV) [9].

Figure 1 illustrates the case of the ^{135}Pr nucleus. The an-

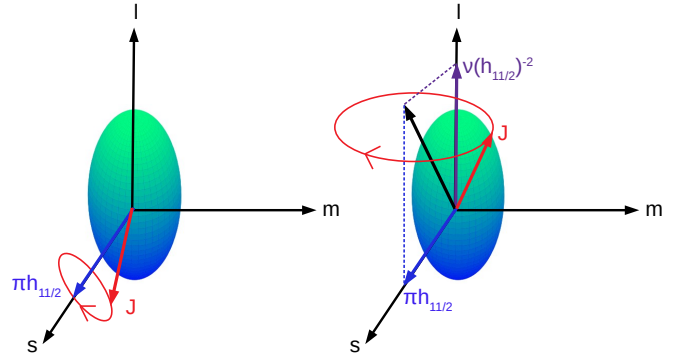


FIG. 1: Angular momentum geometry for (left) transverse wobbling (TW) and (right) the chiral vibration (CV) mode in the body fixed frame, where l , m , and s correspond to the long, medium, and short axis, respectively. \mathbf{J} is the total angular momentum vector. The TW orbit is centered around the s -axis while the CV orbit around the black axis in the l - s plane is the total quasiparticle angular momentum. The quasineutron and quasiproton angular momenta are shown as the violet and blue arrows aligned with the l - and s - axes, respectively. With increasing J , the quasiparticle arrows start following the motion of \mathbf{J} . Figure adapted from Ref. [16].

gular momentum of the odd $h_{11/2}$ quasiproton aligned with the short (s) axis is combined with a pair of $h_{11/2}$ quasineutrons aligned along the long (l) axis. The resulting particle angular momentum vector lies in the l - s plane indicated by the black arrow. The total angular momentum \mathbf{J} precesses around this axis, i.e., it oscillates between the left- and right-handed octants on the sphere of constant angular momentum. With increasing J , the quasiparticle angular momentum starts to follow the motion of \mathbf{J} , due to the Coriolis force. The CV evolves into a strongly anharmonic mode, where \mathbf{J} spends most of the full period in the chiral positions between the l - s

*Electronic address: nsensharma@anl.gov; Present address: Physics Division, Argonne National Laboratory, Argonne, IL 60439, USA

†Electronic address: garg@nd.edu

‡Deceased

§Present address: Physics Division, Argonne National Laboratory, Argonne, IL 60439, USA

¶Present address: Department of Radiology, University of Chicago, Chicago, IL 60637, USA

**Present address: Department of Physical Science, Anne Arundel Community College, Arnold, MD 21012, USA

††Present address: Physics Department, Yale University, New Haven, CT 06511, USA

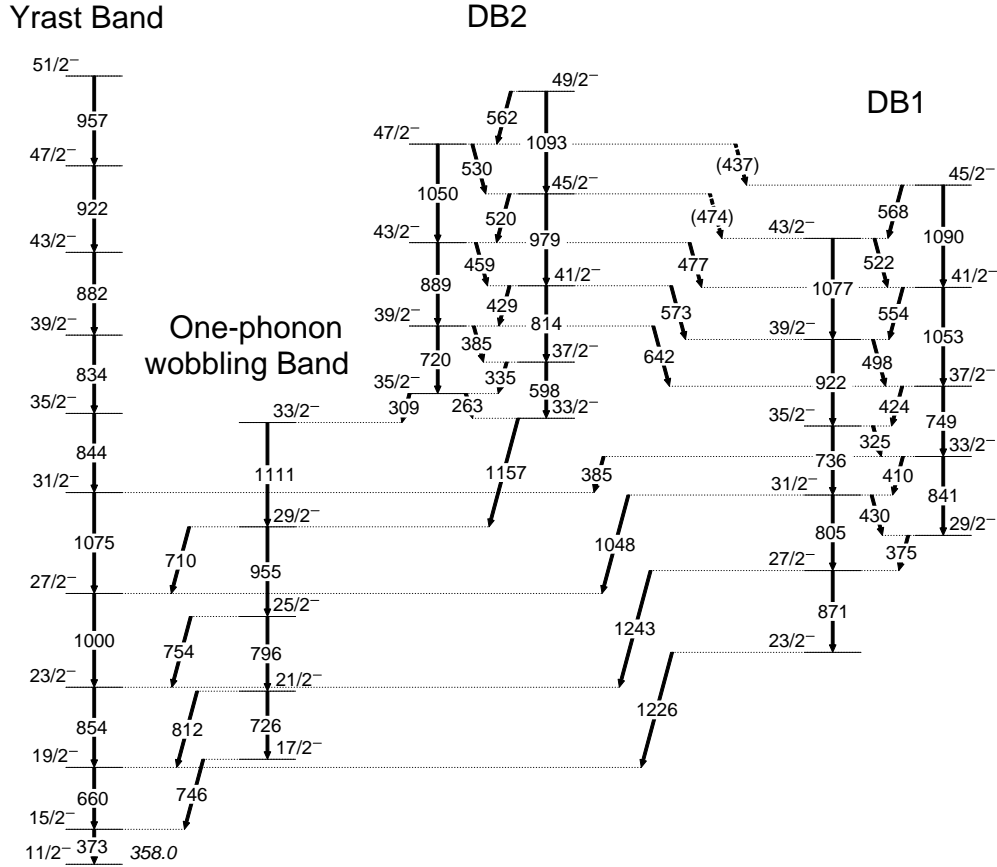


FIG. 2: Partial level scheme of ^{135}Pr developed in the present work. The lowest level shown is an $11/2^-$ isomeric level with $E_x = 358.0$ keV. The five connecting transitions between dipole bands DB2 and DB1 have been newly identified in this work. The tentative γ -ray transitions are given as dotted lines.

and the l - m planes, while rapidly moving over or tunneling through the potential barriers at the two planes (CR).

The chiral configuration evolves through the alignment of the two quasineutrons from the single quasiproton configuration illustrated in the left panel of Fig. 1, which was studied in our previous work [17–19]. There, we demonstrated the appearance of transverse wobbling (TW), which is yet another

manifestation of triaxiality. The present work establishes the existence of chirality in ^{135}Pr . Although the two identifying signatures of triaxial nuclei have been separately established in the aforementioned cases, the simultaneous observation of both in the same nucleus, which proves their mutual relation, had never been demonstrated before.

TABLE I: Initial level energies (E_i), γ energies (E_γ), initial and final spins ($I_i^\pi \rightarrow I_f^\pi$), branching ratios (B.R.), mixing ratios (δ), and adopted multipolarities for the transitions presented in Fig. 2. The last two columns present the experimental transition probability ratios for the in-band transitions of DB1 and DB2 as well as for the $\Delta I = 1$ transitions connecting the two bands.

E_i (keV)	E_γ (keV)	$I_i^\pi \rightarrow I_f^\pi$	B.R.	δ	Mult.	$\frac{B(M1;\Delta I=1)}{B(E2;\Delta I=2)} \left(\frac{\mu_N^2}{e^2 b^2} \right)$	$\frac{B(E2;\Delta I=1)}{B(E2;\Delta I=2)}$
730.7(2)	372.7(4)	$\frac{15}{2}^- \rightarrow \frac{11}{2}^-$	1.00		E2		
1390.3(3)	659.6(4)	$\frac{19}{2}^- \rightarrow \frac{15}{2}^-$	1.00		E2		
1477(5)	746.3(9)	$\frac{17}{2}^- \rightarrow \frac{15}{2}^-$	1.00	$-1.40^{+0.14}_{-0.12}$	M1+E2		
2203.1(5)	811.6(10)	$\frac{21}{2}^- \rightarrow \frac{19}{2}^-$	0.55(1)	$-1.63^{+0.02}_{-0.03}$	M1+E2		
	726.1(10)	$\frac{21}{2}^- \rightarrow \frac{17}{2}^-$	0.45(1)		E2		
2244.4(4)	854.1(4)	$\frac{23}{2}^- \rightarrow \frac{19}{2}^-$	1.00		E2		
2616.4(4)	1226.1(4)	$\frac{23}{2}^- \rightarrow \frac{19}{2}^-$	1.00		E2		
2998.6(4)	754.2(7)	$\frac{25}{2}^- \rightarrow \frac{23}{2}^-$	0.36(1)	$-2.16^{+0.06}_{-0.05}$	M1+E2		
	795.5(6)	$\frac{25}{2}^- \rightarrow \frac{21}{2}^-$	0.64(2)		E2		

TABLE I – *Continued from previous page.*

E_i (keV)	E_γ (keV)	$I_1^\pi \rightarrow I_f^\pi$	B.R.	δ	Mult.	$\frac{B(M1;\Delta I=1)}{B(E2;\Delta I=2)} \left(\frac{\mu_N^2}{e^2 b^2} \right)$	$\frac{B(E2;\Delta I=1)}{B(E2;\Delta I=2)}$
3243.9(4)	999.5(3)	$\frac{27}{2}^- \rightarrow \frac{23}{2}^-$	1.00		E2		
3487.9(4)	1243.4(4)	$\frac{27}{2}^- \rightarrow \frac{23}{2}^-$	0.29(2)		E2		
	871.5(5)	$\frac{27}{2}^- \rightarrow \frac{23}{2}^-$	0.71(5)		E2		
3863(4)	375.1(7)	$\frac{29}{2}^- \rightarrow \frac{27}{2}^-$	1.00		M1+E2		
3954.1(4)	710.2(5)	$\frac{29}{2}^- \rightarrow \frac{27}{2}^-$	0.18(1)		M1+E2		
	955.5(5)	$\frac{29}{2}^- \rightarrow \frac{25}{2}^-$	0.83(5)		E2		
4292.8(4)	1048.4(7)	$\frac{31}{2}^- \rightarrow \frac{27}{2}^-$	0.39(5)		E2		
	804.9(5)	$\frac{31}{2}^- \rightarrow \frac{27}{2}^-$	0.16(2)		E2		
	430.1(7)	$\frac{31}{2}^- \rightarrow \frac{29}{2}^-$	0.45(6)	-0.166(4)	M1+E2		
4319.2(4)	1075.3(4)	$\frac{31}{2}^- \rightarrow \frac{27}{2}^-$	1.00		E2		
4703(4)	384.8(5)	$\frac{33}{2}^- \rightarrow \frac{31}{2}^-$	0.6(1)		M1+E2		
	840.9(6)	$\frac{33}{2}^- \rightarrow \frac{29}{2}^-$	0.22(5)		E2		
	410.2(7)	$\frac{33}{2}^- \rightarrow \frac{31}{2}^-$	0.23(5)	$-0.165^{+0.001}_{-0.002}$	M1+E2	4.34(4)	1.01(1)
5028.3(4)	735.5(5)	$\frac{35}{2}^- \rightarrow \frac{31}{2}^-$	0.22(4)		E2		
	324.8(5)	$\frac{35}{2}^- \rightarrow \frac{33}{2}^-$	0.8(1)	-0.159(2)	M1+E2	15.5(4)	5.3(1)
5065.6(5)	1111.5(4)	$\frac{33}{2}^- \rightarrow \frac{29}{2}^-$	1.00		E2		
5110.9(4)	1156.8(4)	$\frac{33}{2}^- \rightarrow \frac{29}{2}^-$	1.00		E2		
5162.7(5)	843.5(5)	$\frac{35}{2}^- \rightarrow \frac{31}{2}^-$	1.00		E2		
5374.4(5)	308.8(5)	$\frac{35}{2}^- \rightarrow \frac{33}{2}^-$	0.51(2)		M1+E2		
	263.3(4)	$\frac{35}{2}^- \rightarrow \frac{33}{2}^-$	0.49(2)		M1+E2		
5451.8(4)	748.8(5)	$\frac{37}{2}^- \rightarrow \frac{33}{2}^-$	0.230(1)		E2		
	423.6(6)	$\frac{37}{2}^- \rightarrow \frac{35}{2}^-$	0.770(2)	-0.145(3)	M1+E2	7.1(1)	1.19(2)
5709.1(5)	598.2(6)	$\frac{37}{2}^- \rightarrow \frac{33}{2}^-$	0.16(3)		E2		
	335.3(5)	$\frac{37}{2}^- \rightarrow \frac{35}{2}^-$	0.84(2)	-0.049(2)	M1+E2	7.4(3)	0.23(1)
5950.5(5)	922.2(5)	$\frac{39}{2}^- \rightarrow \frac{35}{2}^-$	0.35(2)		E2		
	498.2(6)	$\frac{39}{2}^- \rightarrow \frac{37}{2}^-$	0.65(3)	-0.169(2)	M1+E2	6.9(3)	1.14(6)
5996.8(6)	834.1(4)	$\frac{39}{2}^- \rightarrow \frac{35}{2}^-$	1.00		E2		
6093.9(5)	384.8(6)	$\frac{39}{2}^- \rightarrow \frac{37}{2}^-$	0.5(1)	-0.150(3)	M1+E2	6.3(2)	1.36(3)
	642.2(6)	$\frac{39}{2}^- \rightarrow \frac{37}{2}^-$	0.33(8)	-0.10(6)	M1+E2	0.9(6)	0.03(2)
	719.6(6)	$\frac{39}{2}^- \rightarrow \frac{35}{2}^-$	0.18(5)		E2		
6504.6(5)	1052.8(4)	$\frac{41}{2}^- \rightarrow \frac{37}{2}^-$	0.235(8)		E2		
	554.2(6)	$\frac{41}{2}^- \rightarrow \frac{39}{2}^-$	0.77(3)	-0.055(2)	M1+E2	17.2(8)	0.24(1)
6523.2(5)	814.1(5)	$\frac{41}{2}^- \rightarrow \frac{37}{2}^-$	0.15(2)		E2		
	428.7(8)	$\frac{41}{2}^- \rightarrow \frac{39}{2}^-$	0.67(7)	-0.127(5)	M1+E2	14.3(6)	1.80(7)
	572.9(6)	$\frac{41}{2}^- \rightarrow \frac{39}{2}^-$	0.19(2)	-0.15(3)	M1+E2	1.7(4)	0.16(4)
6878.9(6)	882.1(4)	$\frac{43}{2}^- \rightarrow \frac{39}{2}^-$	1.00		E2		
6982.9(5)	888.9(6)	$\frac{43}{2}^- \rightarrow \frac{39}{2}^-$	0.24(2)		E2		
	459.5(6)	$\frac{43}{2}^- \rightarrow \frac{41}{2}^-$	0.35(3)	-0.206(7)	M1+E2	5.6(2)	1.61(6)
	476.9(6)	$\frac{43}{2}^- \rightarrow \frac{41}{2}^-$	0.41(4)	-0.11(2)	M1+E2	6(1)	0.46(8)
7027.6(5)	1077.1(5)	$\frac{43}{2}^- \rightarrow \frac{39}{2}^-$	0.49(2)		E2		
	522.1(6)	$\frac{43}{2}^- \rightarrow \frac{41}{2}^-$	0.51(2)	-0.138(5)	M1+E2	7.4(3)	0.73(3)
7502.7(5)	979.5(5)	$\frac{45}{2}^- \rightarrow \frac{41}{2}^-$	0.286(4)		E2		
	519.5(7)	$\frac{45}{2}^- \rightarrow \frac{43}{2}^-$	0.71(1)	-0.029(5)	M1+E2	11(2)	0.05(1)
	474.2(6)	$\frac{45}{2}^- \rightarrow \frac{43}{2}^-$			-		
7594.7(5)	1090.1(4)	$\frac{45}{2}^- \rightarrow \frac{41}{2}^-$	0.329(8)		E2		
	567.5(6)	$\frac{45}{2}^- \rightarrow \frac{43}{2}^-$	0.67(2)	-0.059(7)	M1+E2	12(2)	0.18(2)
7801.1(7)	922.2(4)	$\frac{47}{2}^- \rightarrow \frac{43}{2}^-$	1.00		E2		

TABLE I – *Continued from previous page.*

E_i (keV)	E_γ (keV)	$I_i^\pi \rightarrow I_f^\pi$	B.R.	δ	Mult.	$\frac{B(M1; \Delta I=1)}{B(E2; \Delta I=2)} \left(\frac{\mu_N^2}{e^2 b^2} \right)$	$\frac{B(E2; \Delta I=1)}{B(E2; \Delta I=2)}$
8033.1(5)	1050.2(6)	$47^- \rightarrow 43^-$	0.436(5)		E2		
	530.3(8)	$47^- \rightarrow 45^-$	0.564(7)	-0.076(8)	M1+E2	7.7(8)	0.23(2)
	436.8(6)	$47^- \rightarrow 45^-$			–		
8595.5(5)	1092.8(5)	$49^- \rightarrow 45^-$	0.38(2)		E2		
	562.1(6)	$49^- \rightarrow 47^-$	0.62(3)	-0.018(2)	M1+E2	10(1)	0.014(2)
	956.8(4)	$51^- \rightarrow 47^-$	1.00		E2		

The presence of chirality has been mainly associated with the appearance of two closely-spaced $\Delta I = 1$ bands. Further evidence for CR is the relation, $I = \mathcal{J} \omega = \mathcal{J} [E(I) - E(I-1)]$ [1] being a straight line emanating from the origin, which is often reformulated as the staggering parameter $S(I) = [E(I) - E(I-1)]/(2I) = 1/(2\mathcal{J})$ being constant [20]. Selection rules for the electromagnetic transitions have been derived for the special case of one proton particle and one neutron hole occupying the same high- j orbital and coupled to a triaxial rotor with equal minor moments of inertia [21].

In this paper, we present new evidence for the existence of chiral geometry in the ^{135}Pr nucleus by determining the transition-probability ratios for the $I \rightarrow I-1$ transitions between the chiral-partner bands.

II. EXPERIMENT

The experiment was performed using the Gammasphere array at the Argonne National Laboratory. The details of the experiment are similar to those described in Ref. [19]. An 80-MeV ^{16}O beam impinged on an enriched ^{123}Sb target to populate the levels of interest in ^{135}Pr . The target was composed of a $697 \mu\text{g}/\text{cm}^2$ -thick foil of ^{123}Sb with a $15 \mu\text{g}/\text{cm}^2$ front layer of aluminum. A total of 63 Compton-suppressed High Purity Germanium detectors of the Gammasphere array were available and data was acquired in the triple-coincidence mode. Energy and efficiency calibrations were performed using a standard ^{152}Eu radioactive source. To increase our statistics, data from the present run were added to data obtained from the run described in Ref. [19]. The combined total of three- and higher-fold γ -ray coincidence events was 1.52×10^{10} . The RADWARE suite of codes [22] was utilized to analyze the combined data by sorting them into γ - γ coincidence matrices and γ - γ - γ coincidence cubes. A partial level scheme for ^{135}Pr relevant for the focus of this work is presented in Fig. 2.

The dipole bands, labeled as DB1 and DB2 in Fig. 2, were first identified by Refs. [18] and [23], respectively. The present work has confirmed the placement of all the γ rays within the two bands, and has identified five new $\Delta I = 1$ transitions connecting them. The top panel of Fig. 3 presents the spectrum resulting from a coincidence gate on the sum of the three lowest $\Delta I = 1$ newly identified DB2 \rightarrow DB1 transitions (viz. 642.2, 572.9, and 476.9 keV). The middle panel presents the spectrum resulting from the sum of all possible coincidence double gates on the $M1$ in-band transitions within the

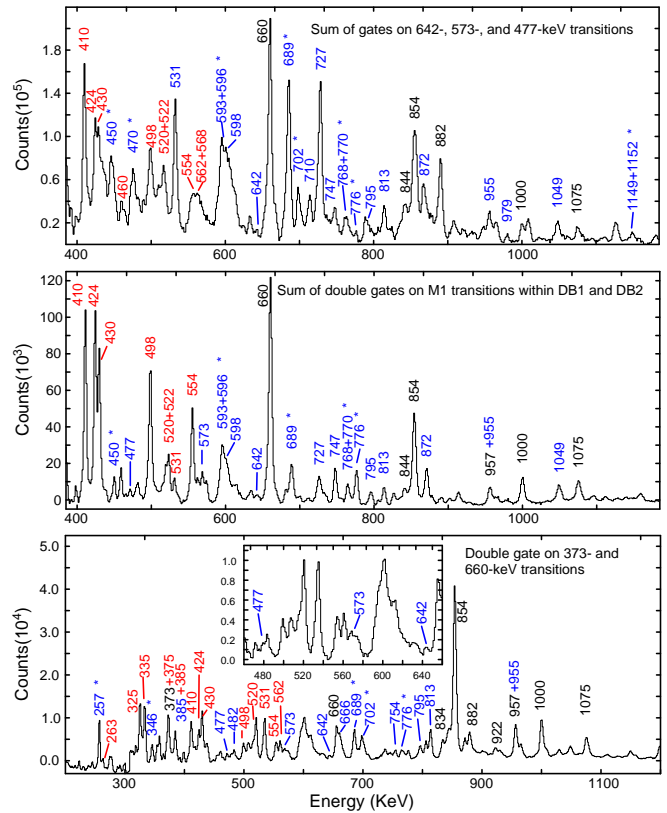


FIG. 3: (Color online) The observed coincidence spectrum resulting from the (top) sum of gates on $E_\gamma = 642, 573,$ and 477 keV, (middle) sum of all possible double gates on the $\Delta I = 1, M1$ transitions within DB1 and DB2, and (bottom) double gate on $373-$ and $660-$ keV transitions. An inset is included in the bottom panel to magnify and clearly display the three lowest DB2 \rightarrow DB1 transitions. The coincident γ -ray energies are marked against the respective energy peaks. The peaks marked in red correspond to the $\Delta I = 1$ in-band transitions of DB1 and DB2. Yrast in-band transitions are marked in black. All other transitions arising from the deexcitation of ^{135}Pr are marked in blue and an (*) is marked on the transitions that were observed, but are not displayed, in the level scheme of Fig. 2.

two dipole bands, and the bottom panel presents coincidence spectrum resulting from a double gate on the $373-$ and $660-$ keV transitions.

Angular distribution measurements have been performed for the three lowest $\Delta I = 1$ interconnecting transitions, and the mixing ratios (δ) corresponding to the lowest χ^2 values

were extracted. The details of the angular distribution measurements are the same as those described in Refs. [19, 24]. Fig. 4 displays the angular distributions for the 642.2-, 572.9-, and 476.9-keV transitions connecting the DB2 and DB1 bands with the corresponding δ value noted on each plot. It is seen that the values of δ are small, implying that these transitions are primarily dipole in character.

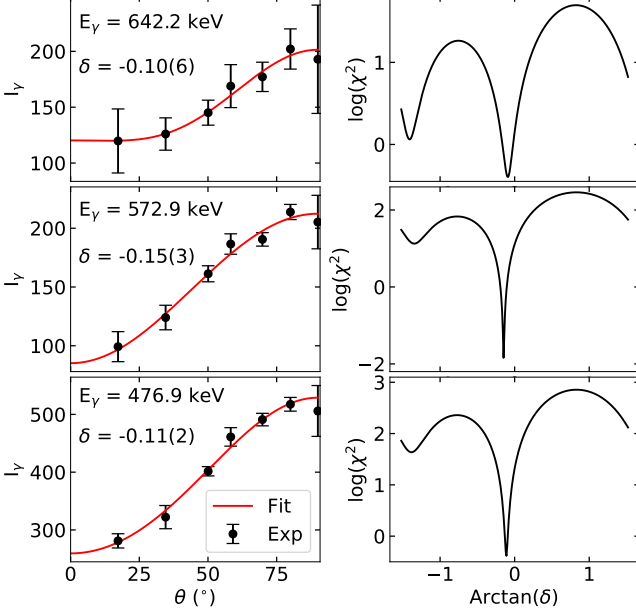


FIG. 4: Angular distribution plots for the three lowest $\Delta I = 1$ transitions connecting the DB1 and DB2 bands. (Left) The experimental points are given as black circles, and the solid red lines are fits to the angular distributions. (Right) Calculated χ^2 values between the theoretical and the corresponding experimental angular distributions presented in the left panel. The minimum χ^2 observed in the plots on the right correspond to the δ values obtained from the angular distribution fits.

The experimental energies for the two dipole bands are displayed in Fig. 5 (a). These DB1 and DB2 bands cross each other with a minimal distance of 17 keV at $I = 41/2$. In accordance, the rotational frequency $\hbar\omega(I)$ in Fig. 5 (b) indicates that DB1 has a surplus of $\approx 2\hbar$ of angular momentum at a given $\hbar\omega(I)$ value. It increases below $I = 41/2$ and stays approximately constant above this value. The mixing ratios extracted from angular distributions were utilized to obtain the transition-probability ratios, $B(E2, I \rightarrow I-1)/B(E2, I \rightarrow I-2)$ and $B(M1, I \rightarrow I-1)/B(E2, I \rightarrow I-2)$, which are listed in the last two columns of Table I, and displayed in the panels (c), (d), (e), and (f) of Fig. 5.

III. DISCUSSION

To understand the nature of the motion, we have carried out calculations in the framework of the quasiparticle triaxial rotor model (QTR) [26–28] for the dipole bands DB1 and DB2, based on the unpaired nucleon configuration $\pi(1h_{11/2})^1 \otimes$

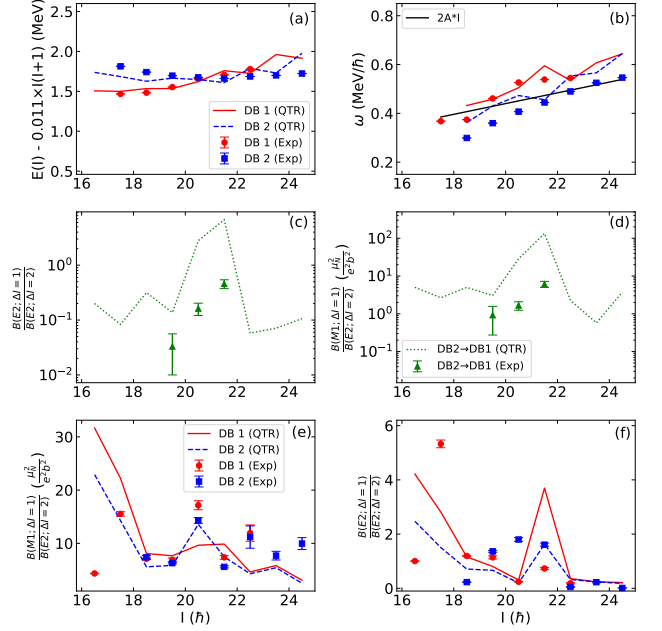


FIG. 5: QTR results in comparison with the experimental data: (a) excitation energies minus a reference, $E(I) - 0.011 \times I(I+1)$, (b) Rotational frequency $\hbar\omega(I - 1/2) = [E(I) - E(I-2)]/2$, where the black straight line shows $\hbar\omega = 2AI$ with $A = 0.011 \text{ MeV}/\hbar^2$, (c) $B(E2; \Delta I = 1)/B(E2; \Delta I = 2)$ and (d) $B(M1; \Delta I = 1)/B(E2; \Delta I = 2)$ ratios for the transitions connecting the DB2 and DB1 bands, (e) $B(M1; I \rightarrow I-1)/B(E2; I \rightarrow I-2)$, and (f) $B(E2; I \rightarrow I-1)/B(E2; I \rightarrow I-2)$ ratios for the DB1 and DB2 bands. Note that the experimental error bars in (a), (b), (e), and (f) are too small to be visible.

$v(1h_{11/2})^{-2}$. In these QTR calculations, the input deformation parameters ($\beta = 0.19, \gamma = 22^\circ$) were determined by the self-consistent adiabatic and configuration-fixed constrained covariant density functional theory (CDFT) [29, 30] with the effective interaction PC-PK1 [31]. The pairing correlations in QTR were taken into account by the standard BCS quasiparticle approximation with the empirical pairing gaps $\Delta_\pi = \Delta_\nu = 12/\sqrt{A} \approx 1.0$ MeV. Setting the energy of the spherical $h_{11/2}$ shells equal to zero, the proton chemical potential $\lambda_\pi = -2.09$ MeV was located at the first level of the $h_{11/2}$ shell, and the neutron chemical potential $\lambda_\nu = 0.96$ MeV was located 0.3 MeV above the midpoint between the fourth and the fifth levels of the $h_{11/2}$ shell. The ratios between the moments of inertia of the rotor were assumed to be of the irrotational-flow type $\mathcal{J}_k = \mathcal{J}_0 \sin^2(\gamma - 2k\pi/3)$ with $\mathcal{J}_0 = 25.0 \hbar^2/\text{MeV}$. In the calculations of the electromagnetic transitions, the empirical intrinsic quadrupole moment of $Q_0 = (3/\sqrt{5\pi})R_0^2 Z\beta$ with $R_0 = 1.2A^{1/3}$ fm and the gyromagnetic ratios of $g_R = Z/A = 0.44$, $g_\pi(h_{11/2}) = 1.21$, and $g_\nu(h_{11/2}) = -0.21$ were adopted. The results of the QTR calculations are displayed in Figs. 5 - 8.

The right-most panels of Fig. 6 display the expectation values $J_i = \sqrt{\langle J_i^2 \rangle}$ of the total angular momentum components with respect to the body-fixed axes. For $I \geq 41/2$, the spin

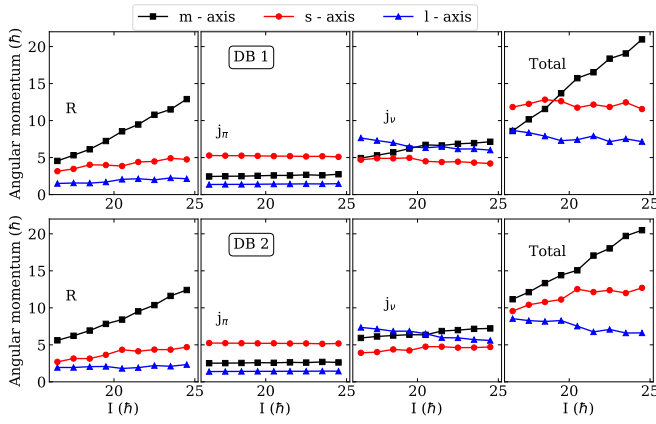


FIG. 6: The root mean square angular momentum components along the medium (m -, black squares), short (s -, red circles), and long (l -, blue triangles) axes of the rotor R , valence proton j_π , valence neutron j_ν , and the total angular momentum J for the DB1 band (top panel) and the DB2 band (bottom panel).

where DB1 and DB2 come closest, $J_s \approx 10\hbar$ and $J_l \approx 10\hbar$, while J_m continuously increases. This is the angular momentum geometry that characterizes chiral rotation as sketched in Fig. 1. The other panels illustrate how the geometry comes about. The l -component is generated by the $h_{11/2}$ quasineutron pair. The s -component is the sum of the $h_{11/2}$ quasiproton and quasineutron contributions. The m -component is mainly generated by the collective angular momentum R , with an increasing contribution from the $h_{11/2}$ quasineutron pair. The real angular momentum composition deviates from the sketch in Fig. 1, because the quasineutron pair does not have the pure hole character of the schematic figure and reacts to the Coriolis force by reorienting toward the m -axis.

Figure 7 complements the display of the mean values of the angular momentum components in Fig. 6. It displays the probability distributions of the total angular momentum J vector and of the quasineutron angular momentum vector j_ν as functions of their angles with respect to the body-fixed frame, where θ is the angle with the l -axis and ϕ is the angle of the projection on the $s-m$ -plane with the s -axis. The distributions represent the classical orbits, as sketched in Fig. 1, where their fuzziness represents the quantum mechanical limit of the concept of classical orbits. The strict definition of these Spin Coherent State (SCS) maps can be found in Ref. [25].

These figures present the chiral angular momentum arrangement, which is schematically illustrated in the right panel of Fig. 1. For $I = 29/2$ and $31/2$, the dipole bands have the character of anharmonic chiral vibrations. The DB1 band has a distribution that corresponds to a squeezed version of the ellipse in Fig. 1 (right) and its reflection through the $\theta = 90^\circ$ plane. The distribution of the DB2 partner corresponds to a squeezed orbit with a larger ϕ amplitude, as is expected for an excited CV. For $I = 33/2, 35/2$ and $39/2$, the distributions of DB1 and DB2 become centered at the left- and right-handed angular momentum arrangements, and gradually move towards the m -axis. The probability distribution of the angular momentum of the one-quasiproton configuration (not

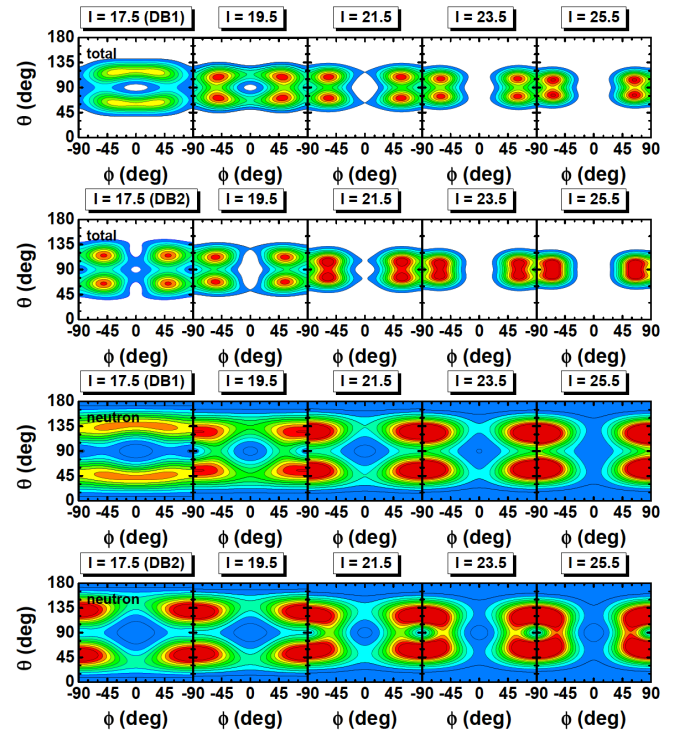


FIG. 7: Distributions of the probability $\mathcal{P}(\theta, \phi)$ for the orientation of the total angular momentum J (upper two panels) and the neutron angular momentum j_ν (lower two panels) with respect to the body-fixed frame (SCS maps) [25] for the DB1 band (top two panels) and the DB2 band (bottom two panels). White, blue, green, yellow, and red are the colors in increasing order of probability.

shown) stays well centered at the s -axis. The angular momentum distribution of the two-quasineutron configuration, on the other hand, has a constant l -component, as indicated in Fig. 1 (right). Additionally, it has s - and m -components, which increase with I .

Figure 5 (a) compares the QTR energies with the experiment. Although there is a good overall agreement, the QTR energies exhibit a signature staggering that is not seen in the experiment. Remarkably, the QTR model reproduces the very small distance of less than 20 keV between the $I = 41/2$ levels. The distributions of DB1 and DB2 in Fig. 7 are very similar. The small difference indicates that the two states must have opposite intrinsic symmetry with respect to the chirality-changing transformation. The chiral-partner bands based on the $\pi h_{11/2} \otimes \nu h_{11/2}$ configuration in the neighboring isotope ^{134}Pr show the same crossing with a distance of about 30 keV between the $I = 14$ levels.

The analog situation for octupole vibrations has been discussed in Ref. [32]. The one-phonon band has a rotationally aligned angular momentum of about $3\hbar$ and odd I , which leads to the crossing of the even- I zero-phonon band. Mixing cannot appear because the bands have different spin and parity.

As seen in Fig. 5 (b), DB1 has a surplus angular momentum of about $2\hbar$, which generates the band crossing. The very small difference in the distance between the $I = 41/2$ levels indicates an opposite symmetry with respect to an in-

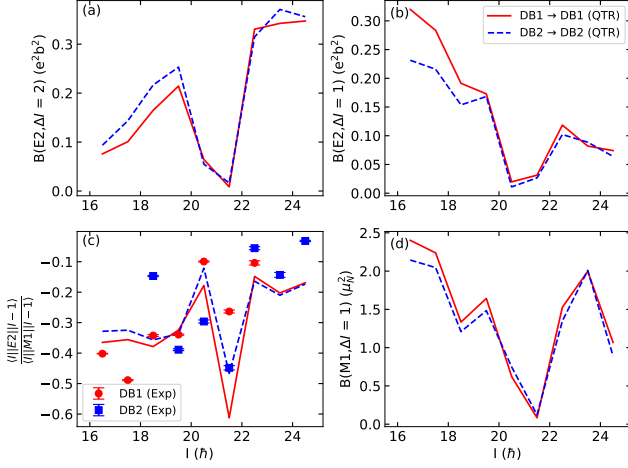


FIG. 8: QTR results for the electric quadrupole transition probabilities for the in-band transitions of DB1 and DB2 (a) $B(E2; \Delta I = 2)$ and (b) $B(E2; \Delta I = 1)$. Panel (c) compares the ratio $\frac{\langle I || E2 || I-1 \rangle}{\langle I || M1 || I-1 \rangle}$ with the experiment. For $I^\pi = 47/2^-$ and $49/2^-$, the ratio is calculated from the predicted QTR transition energies. The magnetic dipole transition probabilities as predicted by QTR are displayed in panel (d).

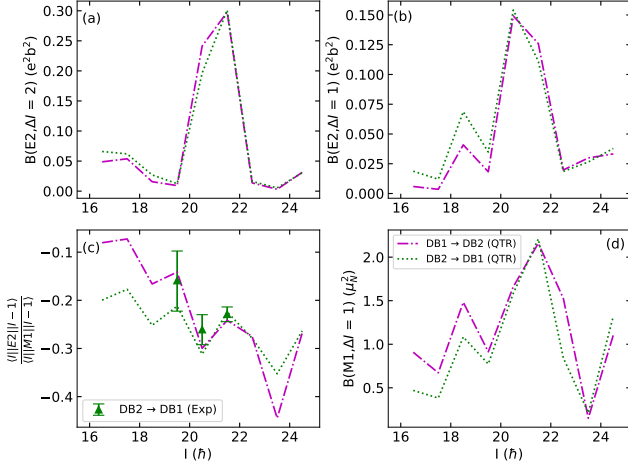


FIG. 9: Same as Fig. 8 but for the $\Delta I = 1$ connecting transitions between the DB1 and DB2 bands.

trinsic transformation for the two states with the same parity and spin. This can only be the change between the left- and right-handed arrangements of the three angular momentum constituents. The details of the band-crossing phenomenon and their relation to the avoided crossing seen in the TW configuration of ^{135}Pr (see Ref. [25]) are yet to be investigated.

The experimental values of $\omega(I)$ presented in Fig. 5(b) approach the relation $\omega = AI$ at large angular momenta, which corresponds to a stable angular momentum component of the quasiparticles in the s - l plane and a small component along the m -axis, as displayed in Fig. 1 (right). The calculations do not reproduce the change of slope, which is consistent with the

continuous increase of the quasineutron m -component seen in Fig. 7. The calculated values of $\omega(I)$ reproduce the difference of about $2\hbar$ of aligned angular momentum, which are characteristic for chiral vibrations [33, 34]. However, they show irregularities near the band crossing, which are not seen in the experiment.

The QTR values for the $B(E2)$ and $B(M1)$ probabilities for the DB1 and DB2 bands displayed in Fig. 8 are very similar, which is expected for chiral-partner bands. The respective values for interband transitions are presented in Fig. 9. With the adopted association of the states within DB1 and DB2, the intraband $B(E2, I \rightarrow I-2)$ values for $I = 41/2$ and $43/2$ are strongly reduced, while the interband values are strongly enhanced, such that their sum smoothly increases with I . The $B(E2, I \rightarrow I-1)$ values behave in the same way, while their sum smoothly decreases with I . The intraband and interband $B(M1, I \rightarrow I-1)$ values (see Figs. 8 (d) and 9 (d)) have, respectively, a minimum and maximum at $I = 43/2$, while their sum slightly decreases with I .

The QTR mixing ratios for the intraband transitions in Fig. 8 (c) follow the experimental ones fairly well. The experimental differences between DB1 and DB2 are larger and opposite compared to the QTR calculations. The QTR values for the interband transitions of $\langle E2 \rangle / \langle M1 \rangle \simeq -0.25$ (Fig. 9 (c)) are close to the experimental ones as well.

From Fig. 5 (e), it is observed that the experimental and theoretical intraband $B(M1, I \rightarrow I-1)/B(E2, I \rightarrow I-2)$ ratios for the DB1 and DB2 bands are similar, supporting the chiral-partner band interpretation. With the above-mentioned association of DB1 and DB2 with the lowest QTR states, the calculated ratios reproduce the experimental ones fairly well, which also holds for the intraband $B(E2, I \rightarrow I-1)/B(E2, I \rightarrow I-2)$ values, displayed in Fig. 5 (f). The fact that the $B(E2, I \rightarrow I-1)$ values are comparable with the $B(E2, I \rightarrow I-2)$ ones is another indication of chiral geometry. The experimental ratios of DB1 and DB2 differ more from each other than predicted by the QTR. The discrepancies reflect the differences of the $\langle E2 \rangle / \langle M1 \rangle$ ratios in Figs. 8 (c) and 9 (c). Further, they may be related to differences of the $B(E2, I \rightarrow I-2)$ values between the chiral-partner bands such as those seen in the neighboring nucleus ^{134}Pr , which have been attributed to a coupling of the orientation degrees of freedom to the shape ones [11].

Figure 5 (c) compares the experimental and theoretical values of the $B(E2, I \rightarrow I-1)_{\text{out}}/B(E2, I \rightarrow I-2)_{\text{in}}$ probability ratios for the $\Delta I = 1$ transitions connecting DB2 with DB1. Fig. 5 (d) presents the same comparison for the $B(M1, I \rightarrow I-1)_{\text{out}}/B(E2, I \rightarrow I-2)_{\text{in}}$ ratios. The QTR energy distance between DB2 and DB1 is less than 150 keV for $I = 39/2, 41/2, \text{ and } 43/2$. A possible non-diagonal matrix element of the order of 100 keV missed by the QTR model Hamiltonian will cause a superposition of the QTR states in DB1 and DB2 that will redistribute the $B(E2)_{\text{in}}$ and $B(E2)_{\text{out}}$ values such that their sum remains the same as seen in Figs. 8 (a) and (b). The same holds for the $B(M1)_{\text{in}}$ and $B(M1)_{\text{out}}$ values as seen in Figs. 8 (d) and 9 (d), respectively. Such a superposition could account for the differences observed in Figs. 5 (c) and (d). However, it would not change the QTR $\langle E2 \rangle / \langle M1 \rangle$ ratios much, which are similar for the interband and intraband

transitions (see Figs. 8 (c) and 9 (c)). Clearly, lifetime measurements would be essential to establish the absolute reduced transition probabilities, and to remove the present ambiguities of being restricted to only ratios.

As observed in Fig. 5, the QTR calculations predict the same reduced transition probabilities for the DB1 \rightarrow DB2 transitions as for the DB2 \rightarrow DB1 ones, which is expected for chiral partners. The absence of DB1 \rightarrow DB2 transitions in the experiment seems to suggest that the two bands exhibit chirality that is more akin to a zero- and one-quantum vibrational state than the static chirality predicted by the QTR model.

The neighboring nucleus ^{134}Pr has been studied in detail in Refs. [9–11]. Compared to ^{135}Pr , it has only one hole-like quasineutron combined with the particle-like quasiproton. Its angular momentum geometry is closer to the “ideal” arrangement of a proton particle, a neutron hole and a $\gamma = 30^\circ$ rotor core, for which the authors of Ref. [21] derived selection rules, which generate the characteristic staggering of the intra and inter band $M1$ transitions. In Ref. [35], the authors demonstrated that the staggering is quickly quenched when the deformation deviates from $\gamma = 30^\circ$. In Ref. [11], the authors interpreted their data for ^{134}Pr in terms of a model that couples the proton particle and the neutron hole with an IBM core and compared it with the QTR model. The fluctuations of the triaxial shape, which the IBM core takes into account, removed the staggering pattern and accounted for the difference between the intra band $B(E2)$ values of the two partner bands. Nevertheless, the analysis of the angular momentum geometry pointed to the presence of “weak dynamical chirality”.

With one proton particle and two neutron holes, ^{135}Pr is asymmetric, which violates prerequisites for the selection rules derived in Ref. [21]. As seen in Figs. 8 and 9, the decay pattern changes to strong intra band and weak inter band E2 and M1 transitions away from the region where the partner bands cross. In the crossing region, strong inter band transitions arise, where the sum of the inter band and intra band values for $B(E2)$ as well as $B(M1)$ changes smoothly with I . The same pattern has been found in the analog asymmetric case of ^{135}Nd , with two proton particles and one neutron hole [7, 8]. The data were well reproduced by the QTR calculations in Ref. [26], where the analysis of the angular momentum geometry demonstrated the chiral nature of the two bands. Lifetime measurements [8] demonstrated that in contrast to ^{134}Pr , the two bands in ^{135}Nd have very similar stretched intra band E2 transitions, indicating a more stable shape. One may speculate that this is the case for the three quasiparticle configuration in ^{135}Pr as well.

In a recent paper, Lv *et al.* [36] questioned our earlier work [18, 19], which reported on the observation of TW in ^{135}Pr . As an important result of the present study – the simultaneous observation of transverse wobbling and chirality – relies on the angular distribution results, in the following we refute their criticisms – both experimental and theoretical – and present additional evidence to further strengthen our arguments.

Reference [36] claims that the mixing ratios, $|\delta|$, for the $\Delta I = 1$ transitions connecting the wobbling bands could also be < 1 , thereby questioning the E2 nature of these transitions

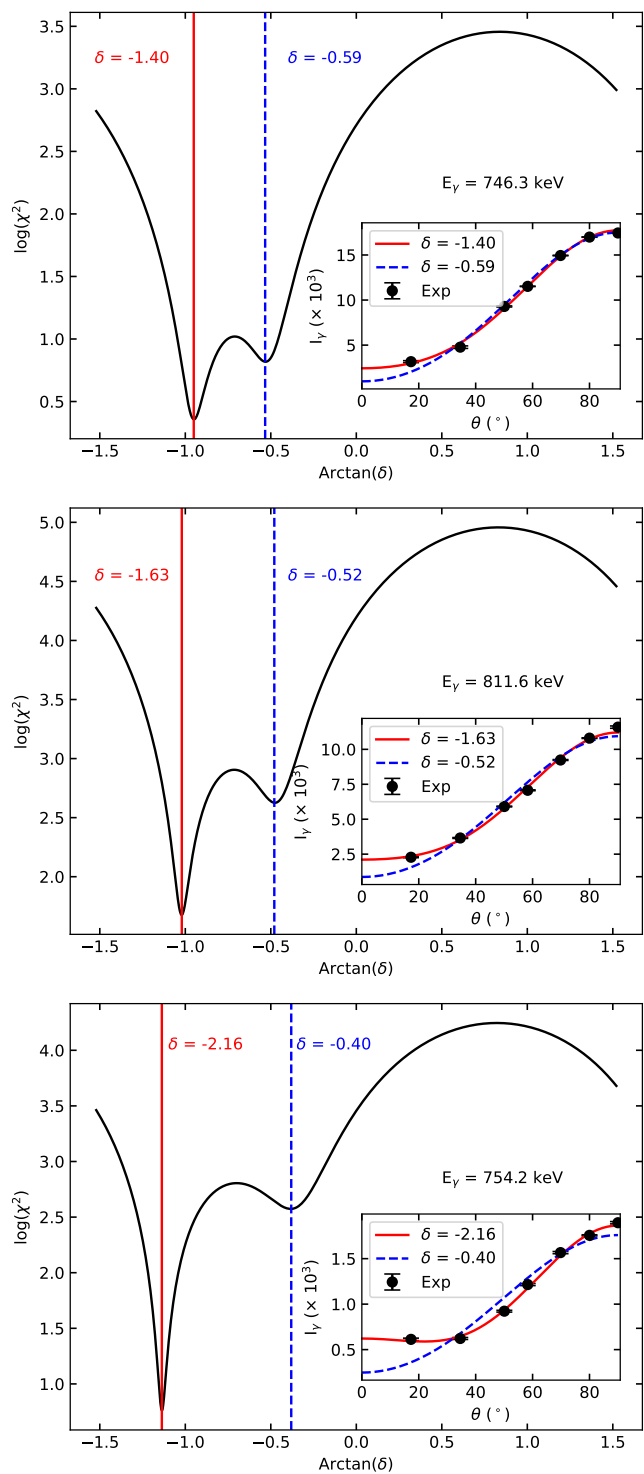


FIG. 10: (Color online) Calculated χ^2 values between the theoretical and experimental angular distributions of the 746-, 812-, and 754-keV transitions in ^{135}Pr (Ref. [18, 19]) as a function of the mixing ratio δ ; the ratio σ/I adopted is 0.2. (Insets) Experimental angular distributions of the 746-, 812-, and 754-keV transitions (black full circles), and calculated distributions with the adopted δ (red solid line) and the other δ corresponding to a higher χ^2 (blue dashed line).

and, hence, the wobbling interpretation of the level sequences. Their argument is that the angular distributions provide two δ values, both of which are equally likely. This observation is in direct contrast to the mixing ratios reported in Refs. [18, 19]. We assert that their claim is erroneous and unfounded. In our measurements, performed with the Gammasphere array, angular distribution information could be obtained at sufficient angles so as to reliably extract both the A_2 and A_4 coefficients of the standard angular distribution expression. This allowed for the mixing ratios to be determined unambiguously by differentiating between the two possible local χ^2 minima, with one of them consistently providing the better fit as determined by the standard χ^2 -minimization techniques. The calculated χ^2 values between theoretical and experimental angular distribution for the 746-, 812-, and 754-keV transitions connecting the wobbling bands as a function of the mixing ratios δ are presented in Fig. 10. Clearly, the data gives only one true minimum in each case, corresponding to the $|\delta| > 1$ value (also reported in Ref. [18]) for these transitions. In the insets, we have presented the experimental angular distributions for these transitions along with the calculated distributions corresponding to the two δ values obtained from solving the quadratic equation (See Eq. 2.46 in Ref. [16]). Just looking at this figure could lead to an erroneous conclusion, as Lv et al. [36] appear to have reached, that the two fits are “similar”; however, the χ^2 minimization process unambiguously gives only one value. The results provided in Refs. [18, 19], thus, clearly establish the predominantly $E2$ character of the transitions connecting the wobbling bands, rendering firm evidence for the occurrence of wobbling motion in this nucleus.

Similar critical comments have been made in [36] about the polarization asymmetries reported in our paper. We wish to point out that the polarization asymmetry measurements were provided merely as a further confirmation of the high $E2$ admixtures established by the angular distribution data, and *not* as a way to determine the mixing ratios therefrom. For the two transitions where it was possible to extract asymmetry parameters, those are positive even beyond the limits of the uncertainties. As reported in our paper, the asymmetry parameters for the transitions identified as “predominantly $E2$ ” are all positive; are closer to those for the known pure $E2$ transitions from the yrast band; and have a sign opposite to that obtained for the 594-keV transition from the signature-partner band to the yrast sequence, which has been designated as “primarily $M1$ ”. Indeed, our procedure, and the associated arguments, are identical to those used in the first reports of wobbling motion in nuclei [37–39]: in the case of the Lu isotopes as well, large negative mixing ratios were found and limited polarization results were employed to confirm the “electric” nature of the wobbling transitions.

The authors of Ref. [36] also wrongly claim that, in the theoretical analyses of Refs. [17–19], the frozen alignment approximation was applied. We want to underline that the experimental results were compared with the QTR calculations, which fully account for the re-orientation of the particle angular momentum. The main difference between the QTR calculations of Ref. [36] and Refs. [17–19] consists in the ratios between the moments of inertia. The calculations in Ref. [36]

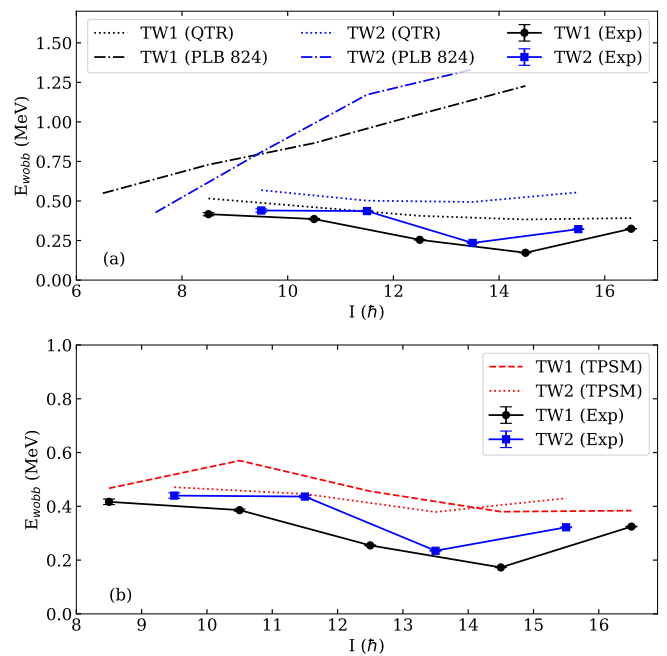


FIG. 11: Wobbling energies, E_{wobb} , as a function of spin for the TW1 and TW2 bands in ^{135}Pr . The experimental values are given as black circles (TW1) and blue squares (TW2). Also shown for comparison are the QTR values from Ref. [19] (black and blue dotted lines) and that from Ref. [36] (black and blue dashed-dotted lines) in the upper panel, and the corresponding TSPM values (dotted and dashed-dotted red lines) in the lower panel.

assume irrotational-flow ratios. The large ratio of four between the m - and s -axes generates an early realignment of the total angular momentum with the m -axis. As a consequence, the energy differences between the lowest band and the next two bands increase with angular momentum in contrast to the experimental energies, as seen in the upper panel of Fig. 11.

In the calculations of Refs. [18, 19], a ratio of about two is assumed, which leads to a later reorientation of the total angular momentum. As a consequence, the relative energies first decrease and then increase, which is the signature of transverse wobbling. As seen in the upper panel of Fig. 11, the angular momentum dependence of the relative energies agrees qualitatively with the experimental ones. The ratio of 2 between the moments of inertia was adjusted such that the QTR energies come as close as possible to the experimental ones.

The TSPM calculations in the lower panel of Fig. 11 evaluated the rotational response microscopically. The similarity between the QTR and TSPM results lends additional credibility to the adjusted ratio of two.

IV. CONCLUSION

In summary, a new pair of chiral-partner bands based on the $\pi(1h_{11/2})^1 \otimes \nu(1h_{11/2})^{-2}$ configuration has been established in ^{135}Pr using a high-statistics Gammasphere experiment with the $^{123}\text{Sb}(^{16}\text{O},4n)^{135}\text{Pr}$ reaction. The predominant

magnetic dipole character of the $\Delta I = 1$ transitions between the chiral-doublet bands has been demonstrated by the precise measurement of angular distributions. Results from QTR calculations are in good agreement with the experimental observations, and demonstrate the chiral partnership. With this observation, both signatures of triaxiality in nuclei–chirality and wobbling–have been evidenced in the same nucleus, putting the triaxial nature of nuclear shapes on a firmer than ever footing.

Acknowledgments

This work has been supported in part by the U.S. National Science Foundation [Grants No. PHY-1713857 (UND),

No. PHY-2011890 (UND), No. PHY-2310059 (UND) and No. PHY-190740 (USNA)]; by the U. S. Department of Energy, Office of Science, Office of Nuclear Physics [Contract No. DE-AC02-06CH11357 (ANL), Grants No. DE-FG02-95ER40934 (UND), No. DE-FG02-97ER41033 (UNC), and No. DE-FG02-97ER41041 (TUNL)]; and by the National Natural Science Foundation of China under Grant No. 12205103. This research used resources of ANL’s ATLAS facility, which is a DOE Office of Science User Facility.

-
- [1] S. Frauendorf and J. Meng, *Nucl. Phys. A* **617**, 131 (1997).
 [2] S. Frauendorf, *Rev. Mod. Phys.* **73**, 463 (2001).
 [3] J. Meng and S. Q. Zhang, *J. Phys. G: Nucl. Part. Phys.* **37**, 064025 (2010).
 [4] J. Meng and P. W. Zhao, *Phys. Scr.* **91**, 053008 (2016).
 [5] S. Y. Wang, B. Qi, L. Liu, S. Q. Zhang, H. Hua, X. Q. Li, Y. Y. Chen, L. H. Zhu, J. Meng, S. M. Wyngaardt, *et al.*, *Phys. Lett. B* **703**, 40 (2011).
 [6] C. Vaman, D. B. Fossan, T. Koike, K. Starosta, I. Y. Lee, and A. O. Macchiavelli, *Phys. Rev. Lett.* **92**, 032501 (2004).
 [7] S. Zhu, U. Garg, B. K. Nayak, S. S. Ghugre, N. S. Pattabiraman, D. B. Fossan, T. Koike, K. Starosta, C. Vaman, R. V. F. Janssens, *et al.*, *Phys. Rev. Lett.* **91**, 132501 (2003).
 [8] S. Mukhopadhyay, D. Almeded, U. Garg, S. Frauendorf, T. Li, P. V. M. Rao, X. Wang, S. S. Ghugre, M. P. Carpenter, S. Gros, *et al.*, *Phys. Rev. Lett.* **99**, 172501 (2007).
 [9] K. Starosta, T. Koike, C. J. Chiara, D. B. Fossan, D. R. LaFosse, A. A. Hecht, C. W. Beausang, M. A. Caprio, J. R. Cooper, R. Krücken, *et al.*, *Phys. Rev. Lett.* **86**, 971 (2001).
 [10] D. Tonev, G. de Angelis, P. Petkov, A. Dewald, S. Brant, S. Frauendorf, D. L. Balabanski, P. Pejovic, D. Bazzacco, P. Bednarczyk, *et al.*, *Phys. Rev. Lett.* **96**, 052501 (2006).
 [11] D. Tonev, G. de Angelis, S. Brant, S. Frauendorf, P. Petkov, A. Dewald, F. Doenau, D. L. Balabanski, Q. Zhong, P. Pejovic, *et al.*, *Phys. Rev. C* **76**, 044313 (2007).
 [12] E. Grodner, J. Srebrny, A. A. Pasternak, I. Zalewska, T. Morek, C. Droste, J. Mierzejewski, M. Kowalczyk, J. Kownacki, M. Kisielinski, *et al.*, *Phys. Rev. Lett.* **97**, 172501 (2006).
 [13] A. D. Ayangeakaa, U. Garg, M. D. Anthony, S. Frauendorf, J. T. Matta, B. K. Nayak, D. Patel, Q. B. Chen, S. Q. Zhang, P. W. Zhao, *et al.*, *Phys. Rev. Lett.* **110**, 172504 (2013).
 [14] D. L. Balabanski, M. Danchev, D. J. Hartley, L. L. Riedinger, O. Zeidan, J. ye Zhang, C. J. Barton, C. W. Beausang, M. A. Caprio, R. F. Casten, *et al.*, *Phys. Rev. C* **70**, 044305 (2004).
 [15] B. W. Xiong and Y. Y. Wang, *Atom. Data Nucl. Data Tables* **125**, 193 (2019).
 [16] N. Sensharma, *Wobbling Motion in Nuclei: Transverse, Longitudinal, and Chiral* (Springer Cham, 2022).
 [17] S. Frauendorf and F. Dönau, *Phys. Rev. C* **89**, 014322 (2014).
 [18] J. T. Matta, U. Garg, W. Li, S. Frauendorf, A. D. Ayangeakaa, D. Patel, K. W. Schlax, R. Palit, S. Saha, J. Sethi, *et al.*, *Phys. Rev. Lett.* **114**, 082501 (2015).
 [19] N. Sensharma, U. Garg, S. Zhu, A. D. Ayangeakaa, S. Frauendorf, W. Li, G. H. Bhat, J. A. Sheikh, M. P. Carpenter, Q. B. Chen, *et al.*, *Phys. Lett. B* **792**, 170 (2019).
 [20] T. Koike, K. Starosta, C. Vaman, T. Ahn, D. B. Fossan, R. M. Clark, M. Cromaz, I. Y. Lee, and A. O. Macchiavelli, *AIP Conference Proceedings* **656**, 160 (2003).
 [21] T. Koike, K. Starosta, and I. Hamamoto, *Phys. Rev. Lett.* **93**, 172502 (2004).
 [22] D. C. Radford, *Nucl. Instrum. Methods Phys. Res., Sect. A* **361**, 297 (1995).
 [23] J. T. Matta, *Exotic Nuclear Excitations: The Transverse wobbling mode in ^{135}Pr* (Springer International Publishing, 2017).
 [24] N. Sensharma, U. Garg, Q. B. Chen, S. Frauendorf, D. P. Burdette, J. L. Cozzi, K. B. Howard, S. Zhu, M. P. Carpenter, P. Copp, *et al.*, *Phys. Rev. Lett.* **124**, 052501 (2020).
 [25] Q. B. Chen and S. Frauendorf, *Eur. J. Phys. A* **58**, 75 (2022).
 [26] B. Qi, S. Q. Zhang, J. Meng, S. Y. Wang, and S. Frauendorf, *Phys. Lett. B* **675**, 175 (2009).
 [27] Q. B. Chen, B. F. Lv, C. M. Petrache, and J. Meng, *Phys. Lett. B* **782**, 744 (2018).
 [28] Q. B. Chen, N. Kaiser, U.-G. Meißner, and J. Meng, *Phys. Lett. B* **807**, 135568 (2020).
 [29] J. Meng, J. Peng, S. Q. Zhang, and S.-G. Zhou, *Phys. Rev. C* **73**, 037303 (2006).
 [30] J. Meng, ed., *Relativistic density functional for nuclear structure*, International Review of Nuclear Physics, Vol. 10 (World Scientific, Singapore, 2016).
 [31] P. W. Zhao, Z. P. Li, J. M. Yao, and J. Meng, *Phys. Rev. C* **82**, 054319 (2010).
 [32] S. Frauendorf, *Phys. Rev. C* **77**, 021304 (R) (2008).
 [33] Q. B. Chen and J. Meng, *Phys. Rev. C* **98**, 031303(R) (2018).
 [34] Q. B. Chen, N. Kaiser, U.-G. Meißner, and J. Meng, *Phys. Rev. C* **99**, 064326 (2019).
 [35] S. Q. Zhang, B. Qi, S. Y. Wang, and J. Meng, *Phys. Rev. C* **75**, 044307 (2007).
 [36] B. Lv, C. Petrache, E. Lawrie, S. Guo, A. Astier, K. Zheng, H. Ong, J. Wang, X. Zhou, Z. Sun, *et al.*, *Physics Letters B* **824**, 136840 (2022).
 [37] S. W. Ødegård, G. B. Hagemann, D. R. Jensen, M. Bergström, B. Herskind, G. Sletten, S. Törmänen, J. N. Wilson, P. O. Tjøm, I. Hamamoto, *et al.*, *Phys. Rev. Lett.* **86**, 5866 (2001).
 [38] D. R. Jensen, G. B. Hagemann, I. Hamamoto, S. W. Ødegård, B. Herskind, G. Sletten, J. N. Wilson, K. Spohr, H. Hübel, P. Bringel, *et al.*, *Phys. Rev. Lett.* **89**, 142503 (2002).

[39] H. Amro, W. C. Ma, G. B. Hagemann, R. M. Diamond, J. Domscheit, P. Fallon, A. Görgen, B. Herskind, H. Hübel, and D. R.

Jensen, *Phys. Lett. B* **553**, 197 (2003).